Astronomy
&
Astrophysics

The role of convection, overshoot, and gravity waves for the transport of dust in M dwarf and brown dwarf atmospheres

B. Freytag[1], F. Allard[1,2], H.-G. Ludwig[3], D. Homeier[4], and M. Steffen[5]

[1] Centre de Recherche Astrophysique de Lyon, UMR 5574: CNRS, Université de Lyon, École Normale Supérieure de Lyon, 46 allée d'Italie, 69364 Lyon Cedex 07, France
e-mail: bernd.freytag@ens-lyon.fr
[2] Institut d'Astrophysique de Paris, UMR 7095: CNRS, Université Pierre et Marie Curie-Paris 6, 98bis boulevard Arago, 75014 Paris, France
[3] Observatoire de Paris-Meudon, GEPI-CIFIST, 92195 Meudon, France
[4] Institut für Astrophysik Göttingen, Georg-August-Universität, Friedrich-Hund-Platz 1, 37077 Göttingen, Germany
[5] Astrophysikalisches Institut Potsdam, An der Sternwarte 16, 14482 Potsdam, Germany

ABSTRACT

Context. Observationally, spectra of brown dwarfs indicate the presence of dust in their atmospheres while theoretically it is not clear what prevents the dust from settling and disappearing from the regions of spectrum formation. Consequently, standard models have to rely on ad hoc assumptions about the mechanism that keeps dust grains aloft in the atmosphere.
Aims. We apply hydrodynamical simulations to develop an improved physical understanding of the mixing properties of macroscopic flows in M dwarf and brown dwarf atmospheres, in particular of the influence of the underlying convection zone.
Methods. We performed two-dimensional radiation hydrodynamics simulations including a description of dust grain formation and transport with the CO5BOLD code. The simulations cover the very top of the convection zone and the photosphere including the dust layers for a sequence of effective temperatures between 900 K and 2800 K, all with $\log g = 5$ assuming solar chemical composition.
Results. Convective overshoot occurs in the form of exponentially declining velocities with small scale heights, so that it affects only the region immediately above the almost adiabatic convective layers. From there on, mixing is provided by gravity waves that are strong enough to maintain thin dust clouds in the hotter models. With decreasing effective temperature, the amplitudes of the waves become smaller but the clouds become thicker and develop internal convective flows that are more efficient in transporting and mixing material than gravity waves. The presence of clouds often leads to a highly structured appearance of the stellar surface on short temporal and small spatial scales (presently inaccessible to observations).
Conclusions. We identify convectively excited gravity waves as an essential mixing process in M dwarf and brown dwarf atmospheres. Under conditions of strong cloud formation, dust convection is the dominant self-sustaining mixing component.

Key words. brown dwarfs – hydrodynamics – convection – waves – stars: atmospheres – stars: low-mass

1. Introduction

Brown dwarfs form like stars and evolve as they cool from stellar-like properties – M spectral type characterized by molecular hydrogen and water vapor formation, chromospheric activity, flares, and magnetic spots – to planet-like properties – T spectral type characterized by methane absorption, electron-degenerate core, and maser emission. With a fully convective interior reaching up to the atmosphere, and a neutral atmosphere offering little interaction with magnetic field lines, they retain larger rotational velocities (≥ 30 km s^{-1}, i.e., $P \leq 4$ h compared to 11 h for Jupiter). This efficiency and the unusually large extent of the convection zone into the atmosphere (up to optical depths of 10^{-3} for M dwarfs) assigns an important role as a cooling and contraction evolution regulator to the atmospheres (Baraffe et al. 1995). Understanding the atmospheric properties has therefore implications for the mass determination of these objects. Some 700 brown dwarfs have been found[1] in the solar neighborhood

and in star-forming regions since the early 90's reaching into ever cooler and lower mass regimes ($T_{\rm eff} \geq 600$ K, $M \geq 5$ $M_{\rm Jup}$).

Atmospheric temperatures are sufficiently low ($T_{\rm gas} \leq 1800$ K, $T_{\rm eff} \leq 2800$ K) for dust particle formation to occur in late-type M dwarfs. These grains should sink under the influence of gravity ($g \approx 10^5$ cm s^{-2}) into deeper layers and vanish from the atmosphere, clearing it from condensable material. However, their near-infrared spectra can only be reproduced when accounting for a strong greenhouse effect (also called a blanketing effect in stellar physics) in the visible layers (Tsuji et al. 1996; Alexander et al. 1997; Ruiz et al. 1997; Leggett et al. 1998, 2001). Classical static model atmospheres have to rely on ad hoc assumptions about the mechanism that keeps dust from settling, or that brings fresh material toward the surface allowing new grains to form (Helling et al. 2008a). The effects of dust formation on the atmospheres of late-type dwarfs have been explored by modeling dust formation in chemical equilibrium with the gas phase using diverse prescriptions of the cloud thickness (Allard et al. 2001; Tsuji 2002; Burrows et al. 2006; Ackerman & Marley 2001). It has been found that the PHOENIX *Dusty* models (Allard et al. 2001) reproduce the infrared emission of

---

[1] Photometry, spectroscopy, and astrometry of M, L, and T dwarfs: http://spider.ipac.caltech.edu/staff/davy/ARCHIVE/index.shtml

late-type M to mid-L dwarfs (i.e., 1700 K $\leq T_{\text{eff}} \leq$ 2500 K) (Leggett et al. 1998, 2001; Ruiz et al. 1997). This indicates that dust forms close to equilibrium in the infrared-line-forming region of these atmospheres ($\tau \approx 10^{-2}$).

On the other hand, late-type L and T dwarfs ($T_{\text{eff}} \leq$ 1400 K) are less affected by photospheric greenhouse effects, but do show evidence – in terms of higher CO and lower NH_3 and CH_4 absorption – of the dynamical upwelling of N_2 and CO gas (Saumon et al. 2006). Cushing et al. (2008) and Stephens et al. (2009) fitted a sequence of the red optical to mid-infrared spectra of early L to mid-T dwarfs using the model atmospheres of Ackerman & Marley (2001) and Saumon et al. (2006). They demonstrated that cloud opacity, adjusted by a sedimentation efficiency factor f_{sed} in these models, affects the spectra of all dwarfs up to early T types, and the observed CO/CH_4 and N_2/NH_3 abundances are indicative of mixing effects equivalent to eddy diffusion coefficients between 10^2 and 10^6 cm^2 s^{-1} in all atmospheres. But this analysis was still not unable to a unique relation between spectral type or T_{eff} and sedimentation efficiency. They also found that the atmospheric parameters derived from best fits to individual spectral regions would frequently infer different results, or be in disagreement with expectations from structural and evolution models. Thus none of the classical static models have reproduced the M-L-T spectral transition satisfactorily.

Attempts have been made to account for atmospheric dynamics in planetary atmospheres, whose models however cat not describe the convection cells and the resulting gravity waves (Marley et al. 2007; Fortney et al. 2006). However, local radiation hydrodynamics (RHD) models of the surface layers of the solar convection have been very successful in reproducing and analyzing the properties of the granulation (Nordlund 1982). In the meantime, various groups have developed similar codes to investigate the atmospheric flows on the sun and other stars (Steffen et al. 1989; Asplund et al. 2000; Skartlien et al. 2000; Stein & Nordlund 2000; Gadun et al. 2000; Robinson et al. 2003; Vögler 2004). Amongst others, these models can describe self-consistently the mixing of material beyond the classical boundaries of a convection zone, as demonstrated for instance for main-sequence A-type stars (Freytag et al. 1996) or for M dwarfs (Ludwig et al. 2002, 2006). A treatment of dust within a 3D simulation of the envelope of an AGB star was included by Freytag & Höfner (2008).

The aim of the current work is to extend the latter simulations into the regime of brown dwarfs, where dust clouds have a strong influence on the photospheric temperature structure, and to quantify the overshoot from the surface convection zone into the atmosphere.

2. Simulations with CO5BOLD

2.1. Numerical radiation hydrodynamics

We computed a sequence of 2D RHD models for a gravity of 10^5 cm s^{-2} (log g = 5) and a range of effective temperatures from 900 K to 2800 K. The models have about 400 × 300 grid points (see Table 1 for details). Most of them are restricted to two dimensions because we are unable to cover the prohibitively long sedimentation and mixing timescales in 3D: a 2D simulation in itself takes about one to three CPU-months to complete. However, a shorter run covering only several dynamical timescales and not trying to cover the longer mixing timescales is feasible in 3D (mt15g50mm00n06).

For this purpose, we used the multi-D RHD code CO5BOLD[2] (Freytag et al. 2002; Wedemeyer et al. 2004) in its local box setup to calculate time-dependent atmosphere models, including the very top layers of the convection zone. To realize this project, we implemented a dust model (see below) as well as dust and low temperature gas opacities.

The code solves the coupled equations of compressible hydrodynamics and non-local radiation transport on a Cartesian grid with a time-explicit scheme. The tabulated equation of state accounts for the ionization of hydrogen and helium, and the formation of H_2 molecules. The 1D hydrodynamics fluxes are computed with an approximate Riemann solver of Roe-type. Because the conditions in the cool objects are almost incompressible, the fluxes are combined non-split, i.e., the fluxes in both the vertical and horizontal directions are computed from the same state (and not after each other) and their contributions are added. In this way, the generation of spurious pressure waves is avoided, which may be produced by a split scheme in regions with large gradients but small divergence in the mass flux.

2.1.1. Dust model

To account for the presence of dust particles, we added terms in the modules for hydrodynamics, radiation transport, source terms, and in handling of boundary conditions. It is impossible to account for all microphysical processes that might play a role in dust formation (Helling et al. 2001; Woitke & Helling 2003) in current time-dependent multi-dimensional simulations. We instead chose a treatment of dust that includes only the most important physical processes. The scheme is based on a simplified version of the dust model used in Höfner et al. (2003). We use a single density field to describe the mass density of dust particles and another for the monomers (gas constituents), instead of four for the dust and none for the monomers as in Höfner et al. (2003) and Freytag & Höfner (2008). Therefore, the ratio of the sum of dust and monomer densities to the gas density is allowed to change, in contrast to the dust description by Höfner et al. (2003). Instead of modeling the nucleation and the detailed evolution of the number of grains, we assume a constant ratio of seeds (dust nuclei) to total number of monomers (in grains or free) per cell. If all the material in a grid cell were to be condensed into dust, the grains would have the maximum radius $r_{\text{d,max}}$, which we have set to a typical value of 1 μm. This is close to the typical particle sizes found for the optically thick part of the cloud deck in solar-metallicity brown dwarfs according to the DRIFT-PHOENIX models of Witte et al. (2009) and according to our own PHOENIX BT-Settl calculations. In both models, particle sizes are determined by a balance between settling speed and turbulent upmixing according to a basic convective overshoot model (cf. Helling et al. 2008b, for a comparison), and are thus in general height-dependent, reaching up to several μm in the deepest cloud layers. For the present models, the value chosen here should allow a reasonable estimate of the dust opacity in the denser parts of the cloud deck. The radius r_{d} of dust grains for given dust mass density ρ_{d} and monomer mass density ρ_{m} is computed from

$$r_{\text{d}} = r_{\text{d,max}} \left[\rho_{\text{d}} / (\rho_{\text{d}} + \rho_{\text{m}}) \right]^{1/3}. \tag{1}$$

Condensation and evaporation are modeled as in Höfner et al. (2003), parameters and saturation vapor curve adapted to forsterite.

---

[2] CO5BOLD User Manual:
http://www.astro.uu.se/~bf/co5bold_main.html

Table 1. Basic parameters of the RHD models (mostly 2D and only one 3D).

Model	p	$n_x \times n_z$	$x \times z$ km $\times$ km	$t_0 - t_1$ 10^3 s	C_{Cour}	s_{in} erg K^{-1} g^{-1}	$T_{\text{eff,sta}}$ K	T_{eff} K	T_{opa} K
mt09g50mm00n10	d	400×430	220×94	90–130	0.30	0.671×10^9	900	897	1000
mt09g50mm00n11	d	400×410	220×90	240–275	0.30	0.671×10^9	900	897	1000
mt10g50mm00n03	d	400×400	240×96	140–195	0.27	0.683×10^9	1000	1030	1000
mt11g50mm00n05	d	400×356	260×92	245–285	0.30	0.690×10^9	1100	1114	1800
mt12g50mm00n01	s	400×336	280×94	110–190	0.40	0.701×10^9	1200	1226	1800
mt12g50mm00n07	s	400×380	280×106	80–150	0.40	0.701×10^9	1200	1228	1800
mt12g50mm00n10	s	400×336	280×94	270–370	0.37	0.701×10^9	1200	1224	1800
mt13g50mm00n01	s	400×270	300×100	80–190	0.40	0.711×10^9	1300	1335	1800
mt13g50mm00n02	d	400×270	300×100	130–200	0.40	0.711×10^9	1300	1336	1800
mt13g50mm00n03	s	400×270	300×100	250–390	0.35	0.711×10^9	1300	1333	1800
mt14g50mm00n01	s	400×270	320×106	40–140	0.40	0.719×10^9	1400	1436	1800
mt14g50mm00n02	s	400×270	320×106	140–280	0.40	0.719×10^9	1400	1437	1800
mt15g50mm00n01	s	400×270	340×113	50–140	0.40	0.728×10^9	1500	1533	1800
mt15g50mm00n02	s	400×270	340×113	150–190	0.40	0.728×10^9	1500	1533	1800
mt15g50mm00n03	s	400×270	340×113	260–380	0.30	0.728×10^9	1500	1533	1800
mt15g50mm00n04	s	300×270	340×113	40–150	0.30	0.728×10^9	1500	1532	1800
mt15g50mm00n06	s	$300^2 \times 270$	$340^2 \times 113$	10–15	0.30	0.728×10^9	1500	1532	1800
mt15g50mm00n07	s	400×300	340×127	70–150	0.30	0.728×10^9	1500	1533	1800
mt16g50mm00n06	s	400×366	352×128	20–190	0.40	0.737×10^9	1600	1648	1800
mt17g50mm00n02	s	400×352	380×133	40–190	0.40	0.747×10^9	1700	1757	1800
mt18g50mm00n07	s	400×343	400×137	40–190	0.40	0.756×10^9	1800	1858	1800
mt19g50mm00n02	s	400×334	420×140	40–80	0.40	0.765×10^9	1900	1953	1800
mt19g50mm00n03	s	400×334	420×140	120–290	0.30	0.765×10^9	1900	1953	1800
mt20g50mm00n05	s	400×362	380×137	40–210	0.20	0.775×10^9	2000	2052	1800
mt22g50mm00n05	s	400×351	400×140	70–150	0.20	0.798×10^9	2200	2247	1800
mt24g50mm00n01	s	400×344	420×144	70–190	0.20	0.825×10^9	2400	2426	1800
mt26g50mm00n01	s	400×353	420×148	70–140	0.20	0.859×10^9	2600	2597	1800
mt26g50mm00n02	s	400×353	420×148	70–140	0.20	0.859×10^9	2600	2611	2800
mt28g50mm00n01	s	400×357	440×157	70–140	0.20	0.905×10^9	2800	2801	2800
mt28g50mm00n02	s	400×380	440×167	40–100	0.20	0.905×10^9	2800	2801	2800

Notes. The columns show model name, numerical precision (single or double), horizontal × vertical resolution, horizontal × vertical size [km × km], time span used for averaging [10^3 s], Courant number, entropy of the material in the deeper layers [erg K^{-1} g^{-1}], effective temperature of the PHOENIX model used for the start file [K], effective temperature of the RHD model versus the average time span [K], and effective temperature of the reference atmosphere used for the opacity table [K].

In the hydrodynamics module, monomers and dust densities are advected with the gas density. However, according to the terminal velocities given by the low-Reynolds-number case of Eq. (19) in Rossow (1978), a settling speed is added to the vertical advection velocity of dust grains, assuming instantaneous equilibrium between gravitational and viscous forces that act onto the grains.

One problem with modeling the dynamics of dust clouds is the span in timescales (short for dust formation and the wave period, long for dust settling and thermal relaxation) and spatial scales (small-scale dust clouds and possible global flows caused by rapid rotation). This is quite similar to simulations of weather patterns on Earth, where global wind systems and local cloud formation interact.

Another problem is the poorly known complex microphysics: a complicated chemical network of molecules with space- and time-dependent abundances can form dust by means of various processes, producing grains with different structures. The dynamical behavior and optical properties both depend on the grain type. Furthermore, depletion leads to a change in the gas composition that affects the equation of state and gas opacities. The current dust model in CO5BOLD is designed to reproduce the essential processes, but cannot account for all details that might possibly play a role.

2.1.2. Equation of state and opacities

The equation of state accounts for the ionization of hydrogen and helium, and the formation of molecular hydrogen. CO5BOLD can deal with the effects of ionization but not with an element composition that depends on space and time. Therefore, the depletion of elements is ignored for the equation of state: the formation of molecules has only a minor effect on e.g., the heat capacity as long as hydrogen exists in the form of H_2. However, molecules play a major role for the opacity, and the formation of molecules depends both on the abundance and depletion of elements. To take this into account, we derived the CO5BOLD gas phase opacities from monochromatic opacity tables, $\kappa(T, P, \nu)$, generated from detailed radiation transfer calculations with the general stellar atmosphere code PHOENIX (Hauschildt et al. 1997). We assume full sedimentation of dust from the gas phase: the removal of condensable material from the gas phase is considered assuming a solar elemental composition in full phase equilibrium at each temperature and pressure point (see Allard et al. 2001; Ferguson et al. 2005). This approximation is close to the conditions prevailing in: i) the lower atmospheric layers that are too hot for dust condensation; ii) the uppermost layers where the gravitational settling depletion is partially compensated by dynamical upwelling of monomers;

and iii) in the cloud-forming layers as confirmed by observations as stated above. The monochromatic gas opacity table was averaged into 5 bins to minimize the computing time but retain the radiative equilibrium properties of the gas.

In contrast to the sophisticated treatment of the gas opacities, we use a simple formula for the dust opacities, which assumes that the large particle limit is valid for all grain sizes and treats scattering as true absorption. The dust opacity [cm^{-1}] is

$$\kappa_d = 3/(2\,\rho_{d,material}\,r_{d,max})\,[\rho_d^2(\rho_d + \rho_m)]^{1/3}, \qquad (2)$$

computed dynamically from the quantities as described for Eq. (1) in each cell of the simulated atmosphere and added to the gas opacity. We concentrate on forsterite grains (Mg$_2$SiO$_4$, 3.3 g/cm^3) that are relatively abundant and provide the greatest contribution to the total dust opacities.

2.1.3. Boundary conditions

The side boundaries of the computational domain are periodic. Usually, an open top is used together with an open bottom boundary conditions for local models that comprise part of a deep convection zone. However, closed boundaries keep the amount of dust and condensable material constant within the computational domain. We therefore used closed boundaries (top and bottom) for all brown dwarf models, although the stellar convection zone should extend to the center of the star. To keep the entropy close to a prescribed value, the internal energy is adjusted for a few grid layers (10 km height) at the bottom of the model. This mechanism acts as an energy source and replenishes the radiative energy losses through the top of the model. This parameter (the value of the entropy plateau s_{in} in the deep convective layers) controls the effective temperature and is taken from the start-up *Dusty* models. Moreover, a drag force dampens downdrafts in these bottom layers.

The top boundary is closed as well, partly to keep material inside. It has a damping zone of about 8 grid points where a strong drag force is applied. Damping at an open boundary did not appear sufficient to keep gravity waves with moderate Mach number (with peak values close to 1) from achieving additional growth to implausibly large amplitudes.

2.1.4. Initial conditions

The thermal structure of a start model is based on a classical 1D stationary stellar atmosphere model produced with PHOENIX assuming hydrostatic equilibrium and radiative plus convective (using the Mixing-Length Theory, Böhm-Vitense 1958) flux equilibrium. We preferred the dust-rich *Dusty* over the dust-free *Cond* models even for lower temperatures where the *Cond* models represent dust-free photospheres, because the resulting effective temperature of the CO5BOLD models agrees very well with the effective temperature of the *Dusty* models (CO5BOLD and PHOENIX models have per construction the same entropy in the deeper layers – not necessarily the same effective temperature). We interpolated the *Dusty* grid points to a finer grid with small or no variation in the grid spacing. To allow sufficient volume for the surface granules to form, we added several points at the bottom by integrating a hydrostatic stratification with constant entropy, taken from the bottom point of the *Dusty* model. At the top, we attached a few points with the internal energy value of the top point in the *Dusty* model, to maintain a sufficient distance between the top of the cloud layers and the top boundary of the computational box.

We enlarged the model in one horizontal dimension to 400 points, and imposed small random velocity fluctuations as seeds for convective instability. Initially, we set a constant fraction of the monomers plus dust mass density divided by the gas density, but which we reduced somewhat empirically in the uppermost layers to account for the partial depletion of material. The relative amount of material in the monomer bin is then determined by the saturation pressure of forsterite. Although the *Dusty* models assume hydrostatic equilibrium, there are small deviations from exact numerical equilibrium in the initial CO5BOLD models. These cause unwanted plane-parallel oscillations that we suppressed by a drag force in the initial phase of each simulation. To dampen these, we applied a strong drag force acting only on plane-parallel motions within the first 100 s. In the following 9900 s, we reduced the drag force to remove remaining plane-parallel residuals. For the remainder of the run (including the interval where we take averages from), we still have a very small but non-zero drag force that dampens plane-parallel vertical and horizontal motions on a timescale of 15 000 s to suppress some modes that grew in early models over very long timescales.

3. Results of the simulations

3.1. Convection and timescales

The quiet solar surface – far away from sun spots – is characterized by a mottled pattern of bright hot rising areas surrounded by dark lanes of cool downflowing material – the so-called granulation at the top of the solar convection zone. Because of their higher surface gravity and lower effective temperature ($\log g = 5$, $T_{eff} \approx 1800$ K), granules on brown dwarfs are about a factor of 10 smaller than their counterparts on the sun ($\log g = 4.44$, $T_{eff} = 5775$ K). Only tiny velocities are required to transport the energy flux through the convection zone, resulting in nearly incompressible low-Mach-number flows (with a maximum vertical rms value ranging from about 0.06 at $T_{eff} = 2800$ K to about 0.003 at $T_{eff} = 900$ K). Accordingly, only small-amplitude pressure waves are present in the brown dwarf models. For comparison, the acoustic timescale (for an up-down-up wave travel) is about 90 s for a 2800 K model and about 60 s at the cool end of our sequence. The Brunt-Väisälä period in the stable layers is about 25 s, while the convective growth time in the unstable layers increases with decreasing effective temperature from around 40 s to about 300 s (minimum values at the "most unstable layers"). The free-fall timescale (to drop one pressure scale height) is around 3 s in the photosphere.

To check the transition from the starting conditions to a quasi-stationary state, we consider time sequences of spatial-averaged quantities, such as temperature, rms velocities, and dust concentration. Starting from random initial fluctuations, the onset of convection takes a few 100 s, longer at lower effective temperatures. A statistically stable pattern develops after a few 1000 s. Wave amplitudes relax on somewhat longer timescales. In contrast, the thermal relaxation time – particularly of the deeper convective layers – is much longer. However, the thermal structure of these layers – an adiabat – remains essentially the same as in the initial model due to our choice of treatment of the lower boundary (keeping the entropy constant instead of imposing a certain flux). In this way, there is no need to cover the complete thermal relaxation time. The longest timescale to be covered is the relaxation time of the dust concentration that has an effect onto the temperature structure. Therefore, each simulation covers a few days of stellar time. The
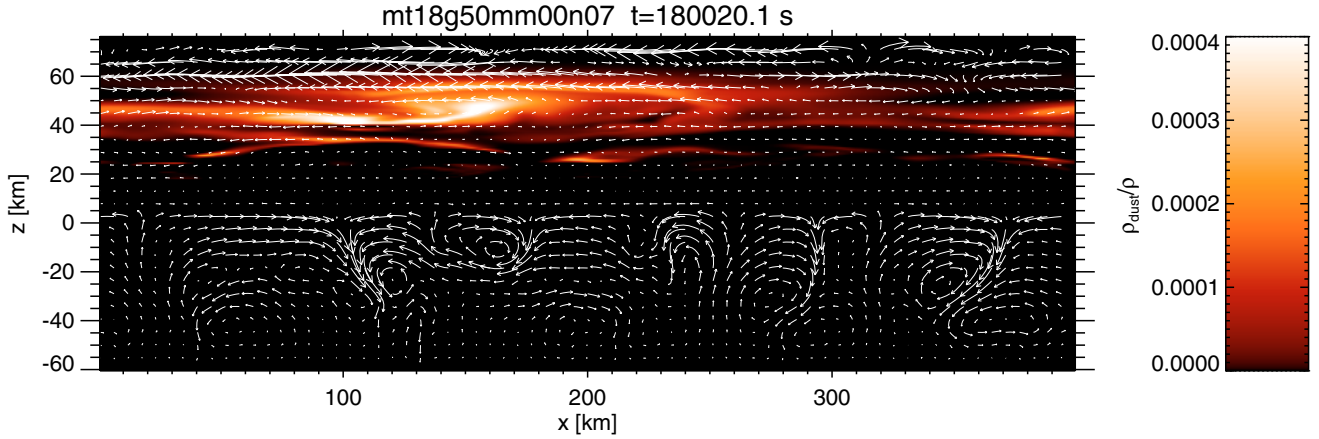
Fig. 1. This snapshot from a brown dwarf simulation with T_{eff} = 1858 K, log g = 5 shows the velocity field as pseudo-streamlines, color-coded according to the dust concentration. The flow in the lower part is due to the surface granulation of the stellar convection zone. The top is dominated by gravity waves.

hydrodynamic time step is about 0.03 s and because of the relatively long radiative relaxation time, we perform multiple (typically 6) hydrodynamical sub-steps per radiation transport step.

Snapshots from our atmosphere simulations are presented in Figs. 1 through 8 while the complete videos are provided as supporting material[3]. Figures 1 and 5 use pseudo-streamlines to visualize the flow field. Figures 2 (for a 1800 K model) and 6 (for a 1000 K model) display sequences of the typical granulation pattern, cool downdrafts occurring in a warmer environment. It is clearly separated from the atmosphere in the upper half of the box that shows inhomogeneities induced by gravity waves. The downdrafts are relatively narrower than in solar granulation (Ludwig et al. 2002, 2006). In the image sequences, the first pair is 20 s apart whereas the last snapshot is taken several minutes later.

The entropy profiles – averaged horizontally over constant height and in time – in Fig. 9 (top left) show a strong increase in the upper atmosphere, with only a minor drop at the top of the convection zone, and an almost flat distribution inside the convection zone. This is indicative of very efficient convection resembling typical conditions in the stellar interior.

3.2. Exponential overshoot

The typical magnitude of the velocity fields can be inferred from the plot of the rms of the vertical velocity versus pressure for various effective temperatures in Fig. 9 (middle panels). The convective velocities fall significantly from the peak value inside the convection zone (on the right) until the top of the unstable layers, and even further into the overshoot region. The scale height of exponentially decreasing overshoot velocities (Freytag et al. 1996; Ludwig et al. 2006) is so small that they do not induce significant mixing in the cloud layers about two pressure scale heights further up. Nevertheless, they are able to mix material across the boundary between stable and unstable layers.

The bottom right panel in Fig. 10 shows the relatively large scale height of the convective velocity at high effective temperatures. This extended overshoot may play a role in the replenishment of dust material. However, the overshoot scale height decreases rapidly with T_{eff} and remains small ($H_v \approx 0.28 H_p$) from about 2200 K on, indicating that this type of overshoot is insignificant for material mixing within the forsterite cloud

---

[3] http://phoenix.ens-lyon.fr/papers/FreytagEtAl2009/
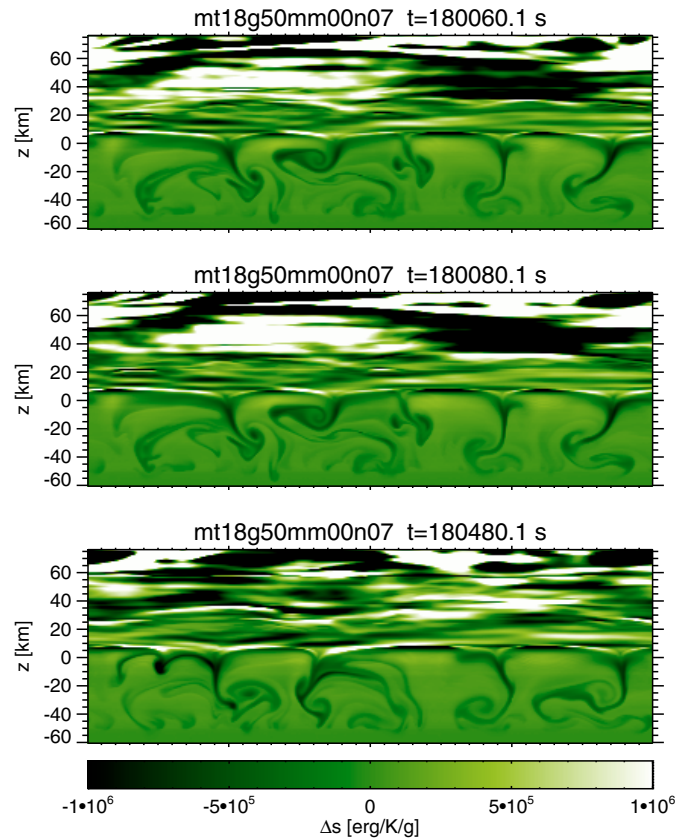
Fig. 2. Three snapshots of the entropy fluctuations (entropy with horizontal average removed) of a brown dwarf model mt18g50mm00n07 with T_{eff} = 1800 K and log g = 5.

layers. On the other hand, for dust types that form at slightly higher temperatures (around 2000 K) as discussed e.g., in Helling et al. (2004) the mixing caused by convective overshoot can play a role.

3.3. Gravity waves

It is instead gravity waves that dominate the mixing of the atmospheric layers (the upper half of the models in Figs. 1 to 8)
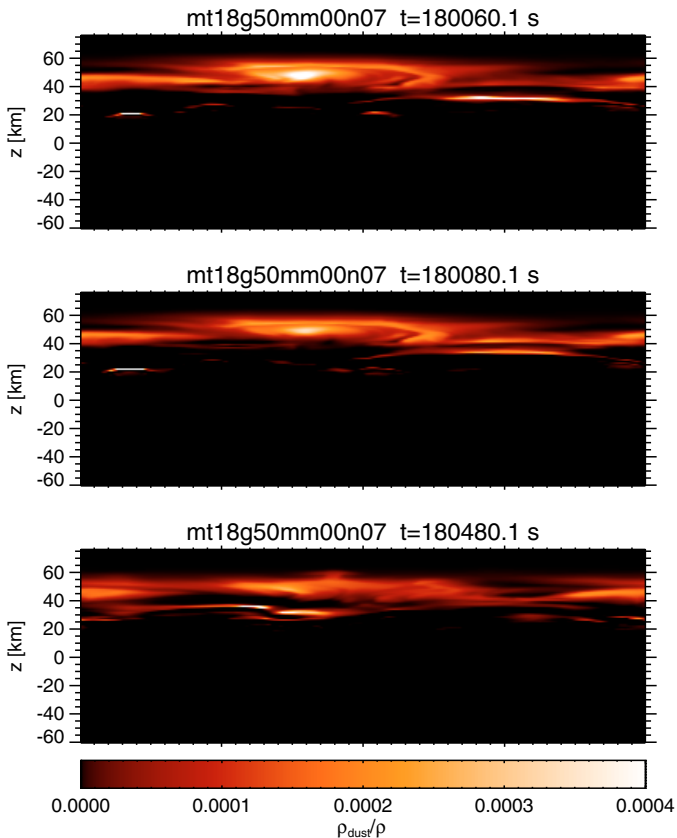
Fig. 3. Three snapshots of the dust concentration of a brown dwarf model mt18g50mm00n07 with $T_{\rm eff}$ = 1800 K and $\log g$ = 5.

Fig. 4. Three snapshots of the concentration of dust+monomers of a brown dwarf model mt18g50mm00n07 with $T_{\rm eff}$ = 1800 K and $\log g$ = 5.

with periods of about 30 to 100 s and amplitudes that increase with height (Fig. 9). Most prominent is the fundamental g-mode, visible particularly in Fig. 6 as a significant brightening between heights of 0 and 20 km. In addition, there are several modes with larger horizontal and vertical wave number. These waves show up together with the first surface granules, well before the downdrafts "hit" the lower boundary. This indicates that the granular flow as such is responsible for the wave excitation, and not artifacts related to the way flows at the lower boundary are handled.

Figures 1 and 3 demonstrate the location of the dust clouds and the effect of the thermal inhomogeneities induced by the gravity waves onto the dust concentration. The generated small amount of vertical mixing (the wave motion is mostly reversible) is sufficient to balance gravitational settling of dust grains and allow dust clouds to form in the hotter models. In addition, dust concentration and cloud thickness are modulated by the waves because of the induced temperature fluctuations.

Atmospheric gravity waves are a common phenomenon. On Earth, they are known to form clouds over e.g., the US midwest plains[4]. Their energy release is involved in heating the exospheres of Jovian planets as observed for Jupiter from Galileo probe results (Young 1998).

Simulations of convection producing gravity waves in stellar conditions have a long tradition (Hurlburt et al. 1986). However, the quantitative estimate of the amplitude and the true detection of internal gravity waves can be a difficult task, even for the well-studied solar case (Belkacem et al. 2009). The detection of

---

[4] Mesonet, I. E. 2007, Gravity Wave Movie: http://mesonet.agron.iastate.edu/cool/
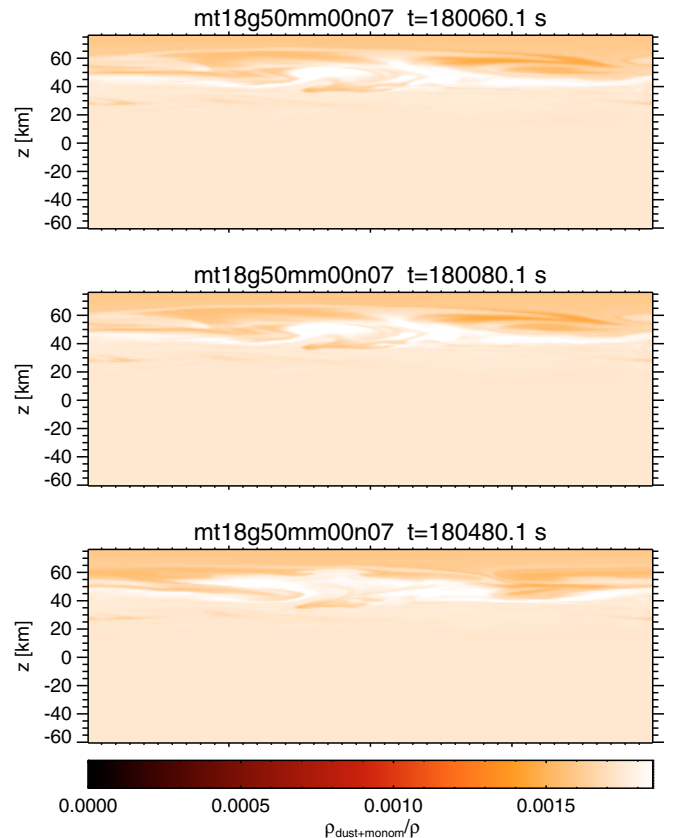
gravity modes that probe the solar core was announced by García et al. (2007).

The initial phases of simulation indicate that gravity waves are generated near the top of the convection zone (see e.g., Dintrans et al. 2005). The gravity waves are produced by nonstationary downdrafts "sucking" at the stable photospheric layers. In this way, the downdrafts are able to inject kinetic energy into the photosphere and to transport some material from there into the deeper convection zone. However, there are no obvious "events" of wave generation as for p-modes in the sun (Goode et al. 1998; Stein & Nordlund 2001) or in the simulations of gravity waves generated by an idealized convection zone embedded between stable layers by Dintrans et al. (2005).

The mixing efficiency of the waves increases rapidly with height – steeper than expected from the mere growths in amplitude caused by the increasing non-linearity. This could be the dynamical updraft mechanism responsible for the upwelling of N_2 and CO gas observed via the enrichment of CO and depletion of CH_4 and NH_3 absorption bands in the spectra of T dwarfs (Saumon et al. 2006; Stephens et al. 2009; Geballe et al. 2009).

3.4. Convection within dust clouds

The fluctuations in the dust concentration in the 1800 K model in Fig. 1 are mainly induced by up and down motions of gravity waves that provide an inefficient mixing that balances the settling of dust grains. However, when the optical thickness of the dust clouds becomes sufficiently high, convective motions *within the dust clouds* start to develop and provide more efficient
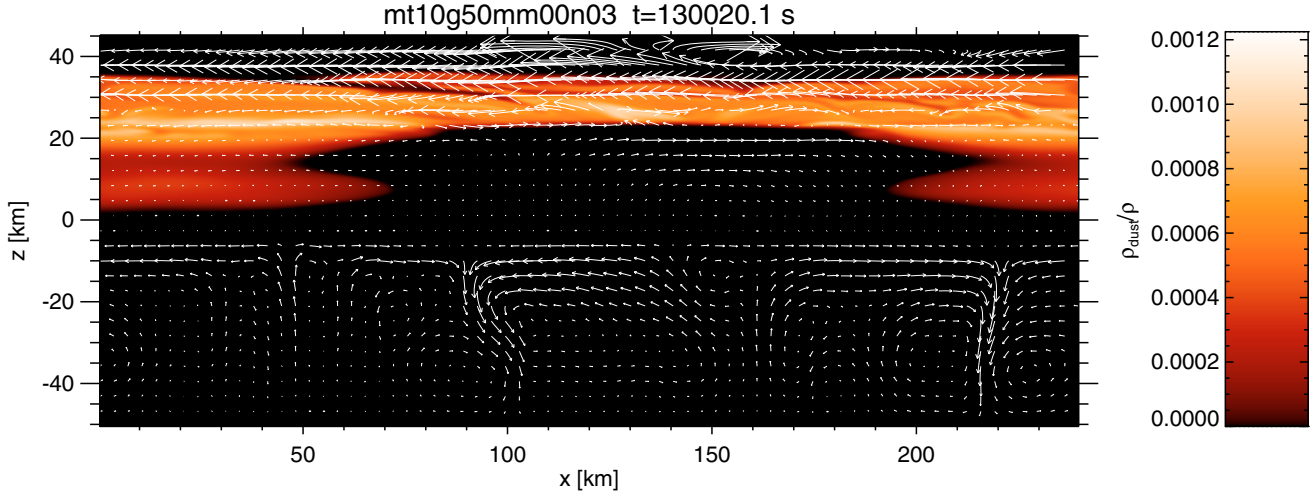
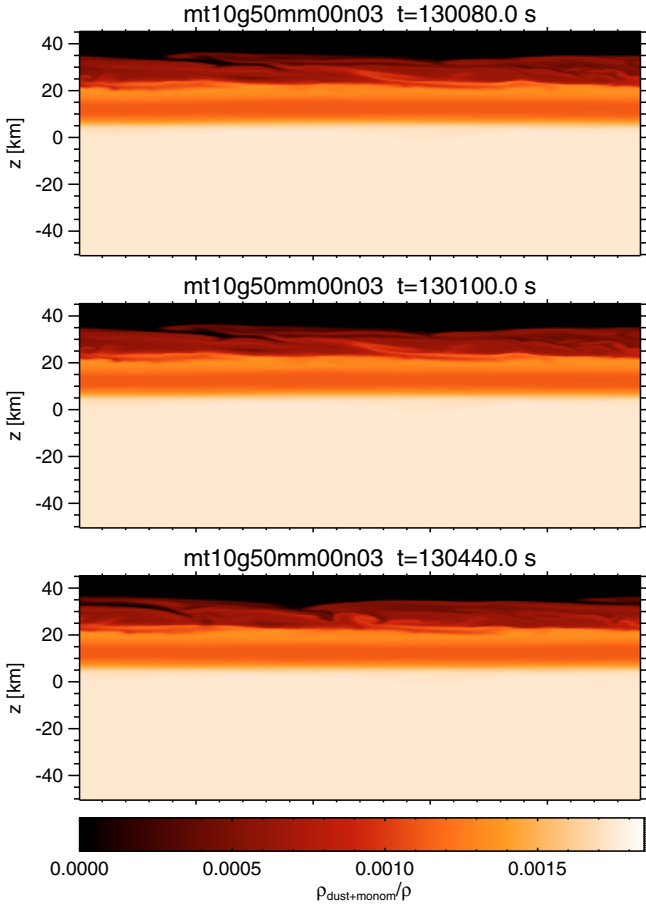**Fig. 5.** As Fig. 1 for a brown dwarf model (mt10g50mm00n03) with $T_{\rm eff} = 1000$ K and $\log g = 5$.
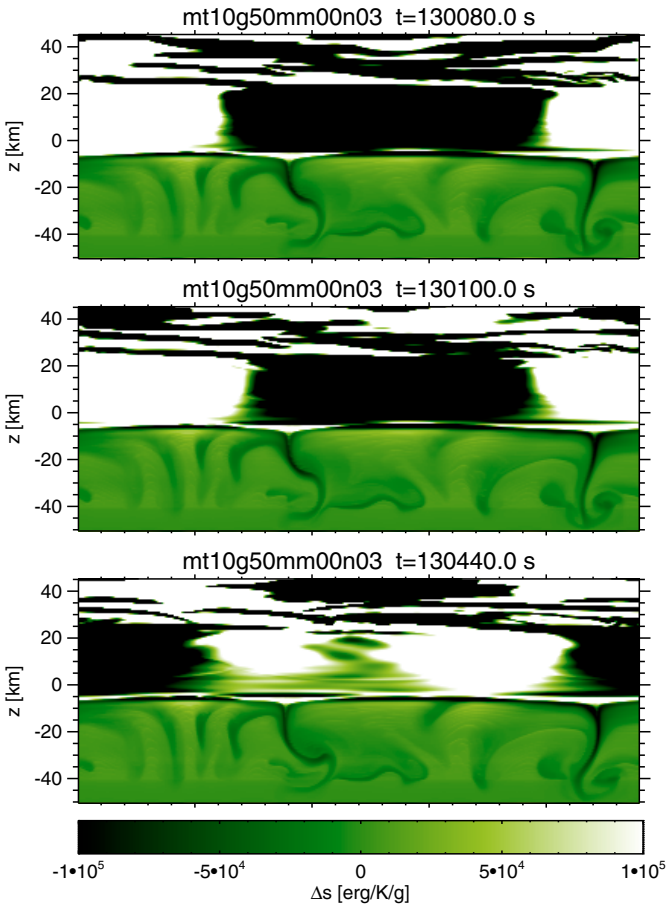
Fig. 6. Three snapshots of the entropy fluctuations of a brown dwarf model mt10g50mm00n03 with $T_{\rm eff} = 1000$ K and $\log g = 5$.
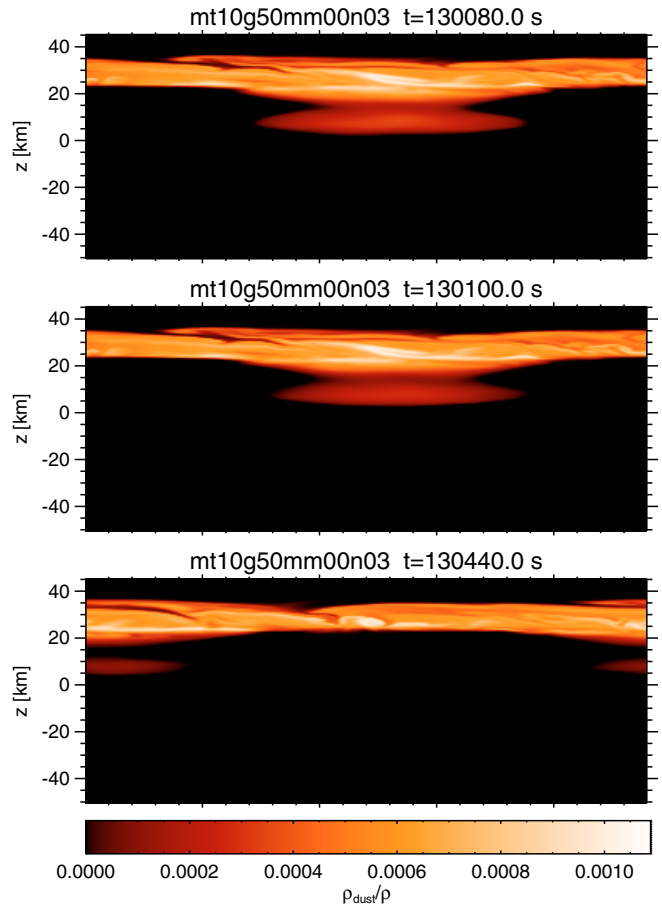
Fig. 7. Three snapshots of the dust concentration of a brown dwarf model mt10g50mm00n03 with $T_{\rm eff} = 1000$ K and $\log g = 5$.

mixing of material (cf. the dust concentration of the 1000 K model in Fig. 7). However, in the snapshots the fluctuations and flows due to the waves somewhat obscure the dust cloud convection, whereas the overturning motions are clearly visible in movies and have a different signal in a k-ω diagram.

There are different intermittent processes: occasionally, material from the dust layers is dredged up to the layers with relatively low dust concentrations above the clouds. The grains quickly fall back. But monomers can remain a while, until they condense into dust at the top of the cloud deck. The cloud layer

Fig. 8. Three snapshots of the concentration of dust+monomers of a brown dwarf model mt10g50mm00n03 with $T_{\rm eff} = 1000$ K and $\log g = 5$.

thickness varies not only with the wave on a timescale below one minute but also in irregular cycles on timescales of hours. The irregularity and amplitude increases with decreasing effective temperature.

During the initial phases of a simulations, a violent thin cloud convection zone develops for a limited time until the model is relaxed. This phenomenon relates to differences between our start model and the final outcome. However, on actual brown dwarfs large-scale flows might cause an imbalance in the local dust concentration that leads to a similar localized enhanced cloud activity.

3.5. Dust and stratification

In the top left panel in Fig. 10, we show the location of the dust clouds (circles connected by vertical lines) relative to the underlying gas convection zone (located below the crosses).

The mixing processes within the dust cloud layers have different height regimes. At the bottom of the dust clouds, the temperature varies around the condensation value but there is little mixing. With our dust scheme, which assumes the presence of nuclei everywhere where dust or monomers are present, dust forms and evaporates during these temperature cycles (see the dust concentration at $z \sim 10$ km in Fig. 7). The dust formation would be more difficult if new dust grains had to nucleate, because that would require some level of supersaturation. Within the clouds, material is mixed by gravity waves and/or convection (depending on effective temperature). The top of the clouds

is sharp but inhomogeneous due to (sometimes braking) waves and cloud convection. Above the cloud layers, there are still mixing flows that try to equalize the concentration of monomers with height. The concentration value depends on the efficiency of mixing, dust formation, and dust settling in the cloud layers below (Fig. 9, bottom panels).

Dust clouds have a strong effect on the thermal structure (Fig. 9, top right panel): there is a fairly shallow temperature slope beneath the cloud layers with values of about 1600 K because of the greenhouse effect, a rapid drop within the clouds due to the large dust opacities, that can even drive cloud convection, low temperatures (with values around 1000 K and small variations) in the mostly dust-free upper atmosphere, and in some cases a small increase at the top of the models of about 100 K because of the dissipation of kinetic wave energy. At some height above the cloud, gravitational settling of dust grains becomes more efficient than mixing. The dust density drops rapidly and with it dust opacity and temperature, causing a rather sharp (but variable in space and time) upper boundary of the clouds. The concentration of dust and monomers (material that potentially can form dust) in Figs. 4 and 8 shows complete mixing in the convection zone, depleted layers at the top of the atmosphere (due to gravitational settling), and a partially mixed region in-between.

3.6. Effective temperature dependency

We summarize the dependence of our model properties on effective temperature in Fig. 10. The upper right panel shows that the atmospheric velocities (squares) do not follow the monotonic decrease in the convective velocities (crosses) up to the lowest effective temperatures, but rise after a minimum around $T_{\rm eff} = 1900$ K. However, the cloud thickness (top left panel) and cloud mass (bottom left panel) increase monotonically with decreasing effective temperature. The cloud extension with $T_{\rm eff}$ is slightly erratic because the models have not perfectly converged. At higher effective temperatures, the thin see-through clouds allow a view of the upper layers of the convection zone (plus signs in both top panels), while at the lower-$T_{\rm eff}$ end most of the cloud mass sits below the visible layers.

The rms vertical velocity, which is often used in static model atmospheres to estimate line broadening, non-equilibrium chemistry due to mixing, or cloud formation, can be parametrized as a function of effective temperature for our sequence of 30 models. Hence, with the logarithmic normalized temperature $x = \log(\min(\max(T, 900\ {\rm K}), 2800\ {\rm K})/1\ {\rm K})$, we obtain for the velocity scale height of the wave amplitude (bottom right panel in Fig. 10)

$$H_{\rm v}/H_{\rm p} = \max(2.855, -43.1 + 14.34\,x), \qquad (3)$$

and for the logarithmic ratio of maximum convective velocity to wave amplitude extrapolated to this layer

$$\log r_{\rm v} = \max(835.684 - 828.156x + 273.426x^2 - 30.1148x^3, \\ -25.496 + 7.1104x), \qquad (4)$$

where the first expression in the max functions is a good fit for temperatures below approximately 2000 K, and the second expression for temperatures above. To recover a crude estimation of the mixing efficiency based on these formulae, we propose to compute the amplitude $V_{\rm max}$ and position $P_{\rm max}$ of the maximum convective velocity with e.g., the Mixing-Length Theory, to add $\log r_{\rm v}$ to the logarithmic velocity amplitude, and to
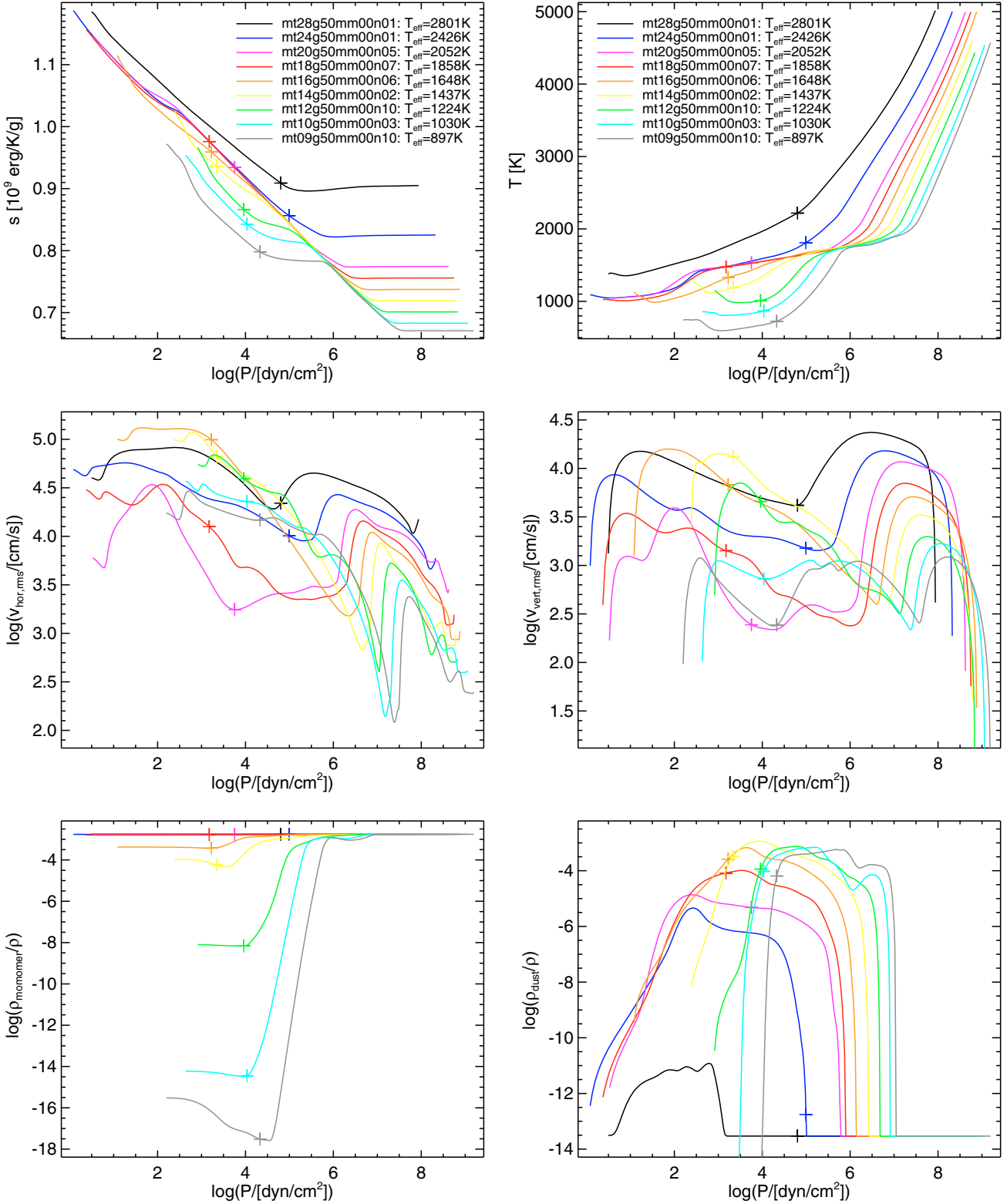
Fig. 9. Various averaged quantities versus logarithm of pressure: *top left*: mean entropy for various effective temperatures and $\log g = 5$. The plus signs mark the layers with Rosseland optical depth 10^{-2}. The legend is the same in all panels. *Top right*: mean temperature. *Middle left*: logarithm of rms horizontal velocity. *Middle right*: logarithm of rms vertical velocity. *Bottom left*: logarithm of monomer concentration. *Bottom right*: logarithm of dust concentration.

extrapolate from this starting point the wave amplitude with H_v/H_p into the atmosphere,

$$\log V = \log V_{\max} + \log r_v - (\log P - \log P_{\max})/(H_v/H_p), \quad (5)$$

where P is the pressure. We note, that for the models with $T_{\rm eff} = 900$ K and 1000 K the velocities drop after reaching a maximum of about 10 m s^{-1}, while the rise in the velocities of the hotter
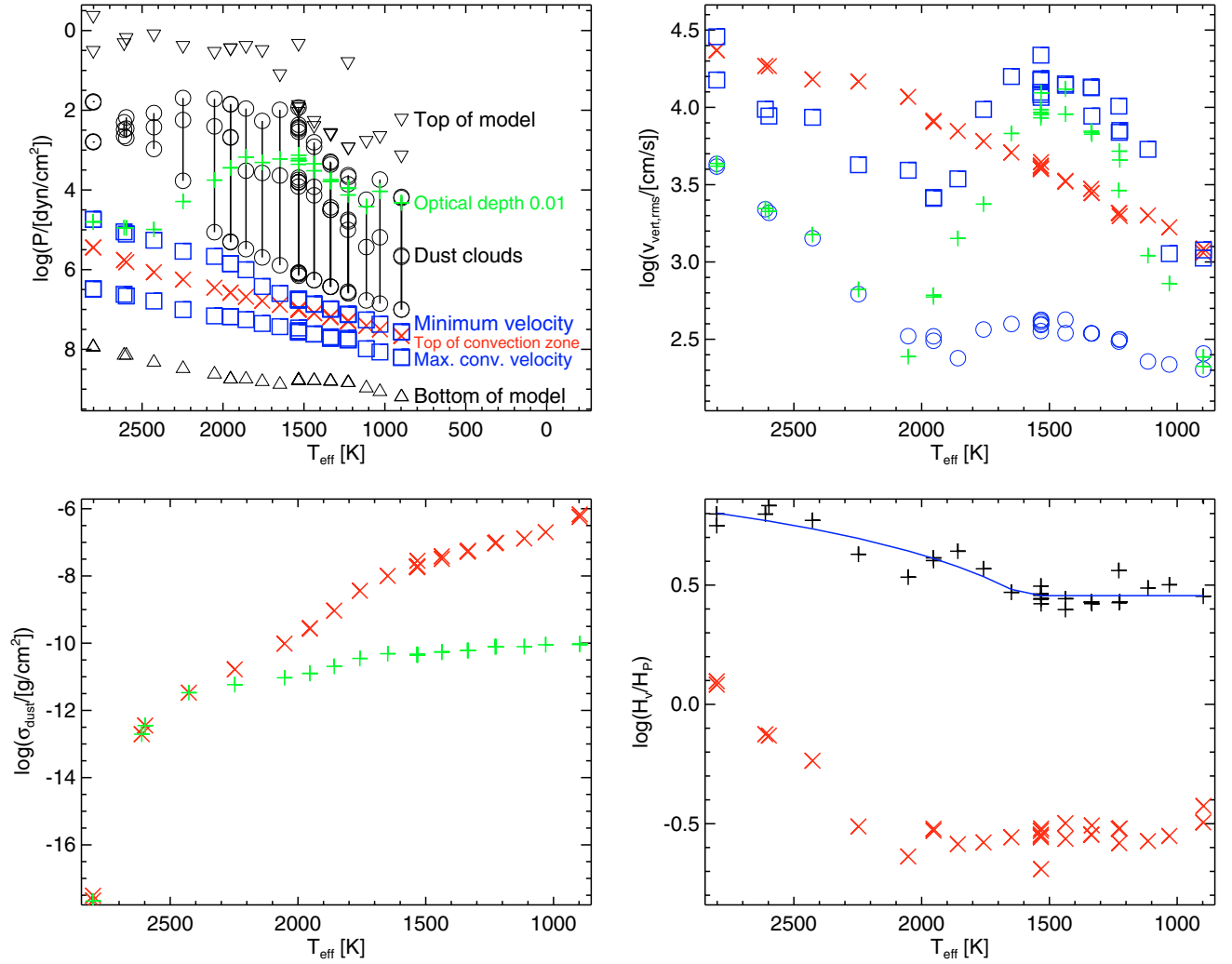
Fig. 10. Various quantities plotted versus effective temperature for all models in Table 1. *Top left; logarithm of pressure for various points of interest*: black triangles: top and bottom of each model, red crosses: top of convectively unstable layers, lower set of blue squares: point with maximum convective velocity $v_{vert,rms}$, black circles: upper and lower boundary of cloud layers (region where the dust concentration lies above 10^{-6}) and point of maximum dust concentration, green plus signs: layers with $\tau_{Rosseland} = 10^{-2}$. *Top right; rms value of vertical velocity $v_{vert,rms}$*: red crosses: maximum convective velocities, blue squares: maximum wave velocities, blue circles: minimum velocity in between, green plus signs: velocity at $\tau_{Rosseland} = 10^{-2}$. *Bottom left; total amount of dust*: red crosses: total amount of dust in model, green plus signs: dust above layers with $\tau_{Rosseland} = 10^{-2}$. *Bottom right; scale height of rms of vertical velocity*: black plus signs: approximate scale height of increase of wave velocities with height, blue line: fit according to Eq. (3), red crosses: scale height of exponentially declining overshoot velocities.

models appears to be limited only by the top of the computational domain.

The rise of velocities above the convection zone becomes steeper with decreasing temperature (bottom right panel in Fig. 10). But the amplitudes in the atmosphere (Figs. 9 and 10, top right) fall from models with high effective temperatures to models with $T_{eff} \approx 2000$ K.

For even cooler models, the amplitudes increase again. This increase is not because of the velocities in the underlying gas convection zone that decline steadily as effective temperature decreases. Instead, below 2000 K, the clouds have grown to such a large vertical thickness and density that cloud convection begins – with effects onto the atmospheric velocities and temperature structure that increase with further decreasing effective temperature. We attribute the rise in velocity for

low-temperature models mainly to the emergence and growth of cloud convection.

Therefore, the dust clouds also affect the waves: when they become extended enough they split the atmospheric cavity for gravity waves into two separate zones by generating an entropy plateau within the atmosphere (Fig. 9). At T_{eff} below about 1000 K, the gravity waves are trapped mainly inside the region between the two convection zones. The layers above the dust convection zone exhibit only small wave amplitudes.

The convective-radiative boundary becomes steeper, hence harder, with lower effective temperature, easing the gravity wave generation. In addition, there is a slight change in the topology of granules: in the hotter models, the downdrafts that delimit the granules are of roughly similar strength and merge occasionally, while in the cooler models just a few (2 or 3) "super downdrafts" dominate and absorb the smaller ones that form on

top of the granules. This process occurs with higher frequency than would be expected if the merging type were the same as in the hot models – with possible consequences for the interaction between convection and waves.

## 4. Discussion

4.1. Parameter dependence

The details of the wave generation process and the type, amplitude, interaction, long-term evolution, and spectrum of the waves are complex and may have connections to numerical settings. Some small-amplitude pressure waves in the hottest models are emitted from the non-stationary downdrafts as expected and become invisible at intermediate temperatures. However, in the lowest-temperature models ($T_{\rm eff} \leq 1300$ K) the signature of high-frequency p-modes unexpectedly showed up in the pressure fluctuations, where g-modes and convection have only a small signal due to their nearly incompressible nature and small amplitude. The p-modes contribute to the velocities only close to the very top of the computational box. Their amplitude depends sensitively on viscosity and the position of the top boundary. They vanish, when the Courant number is reduced from 0.4 to about 0.3, depending on other model details (the usual stability criterion sets an upper limit at 0.5 for the 2D models). The models that we used for our final analysis show no or only traces of these p-modes.

An early version of the models showed (in addition to the "normal" spectrum of gravity waves that occur as soon as convection sets in) after the simulation had run for a long time a slowly exponentially growing gravity wave in the fundamental mode. It grew until the code crashed because of too steep velocity gradients at the top of the box. It had relatively little effect on mixing, but induced temperature fluctuations modulating the dust concentration. Limiting the model depth, and using both a finer vertical grid and a smaller Courant number prevented an exponential growth of the mode. However, the mode itself is still present and quite prominent in the cooler models.

We varied several numerical parameters to check their influence. By considering a pair of models with $T_{\rm eff} = 1300$ K, one in single, the other in double precision, we found hardly any difference at all in the resulting mean properties (velocities and temperature). However, at $T_{\rm eff} \leq 1100$ K the density fluctuations in the convection zone become so small that they cannot be resolved properly using single precision: after a transient phase, convection dies out leaving only small-scale low-amplitude velocity fluctuations in the "convection zone" that are due to roundoff errors. Therefore, all runs with $T_{\rm eff} \leq 1100$ K were performed in double precision from the initial tests on.

For a 1500 K model, we decreased our standard horizontal resolution by going from 400 to 300 horizontal grid points and found no noticeable difference in the mean structures, although the thin convective downdrafts and some small-scale cloud structures are somewhat less well resolved.

For the generation of our binned opacity tables, the bins were optimized for three reference atmosphere cases ($T_{\rm eff} = 1000$ K, 1800 K, and 2800 K with $\log g = 5.0$ and solar metallicity). The resulting tables are most accurate for model parameters close to these values. In Fig. 11, we show the temperature structure of two models with $T_{\rm eff} = 2600$ K using an opacity table made with a 1800 K reference atmosphere in mt26g50mm00n01, and with a more appropriate 2800 K reference atmosphere in mt26g50mm00n02. The resulting differences are most important
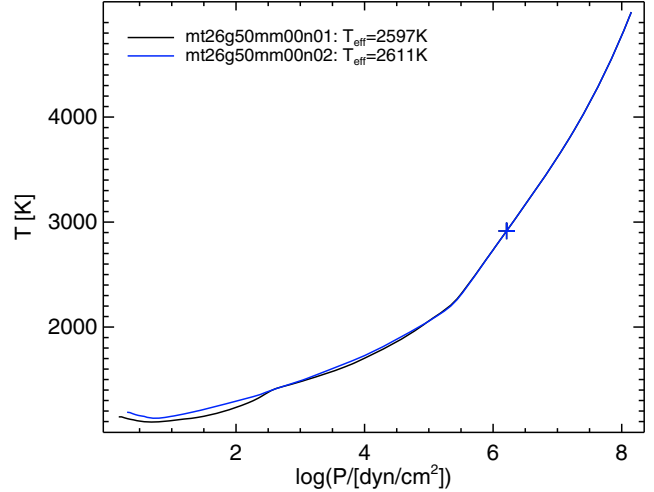
Fig. 11. Mean temperature versus logarithm of pressure for two models with $T_{\rm eff} \approx 2600$ K, $\log g = 5$, but different opacity tables.
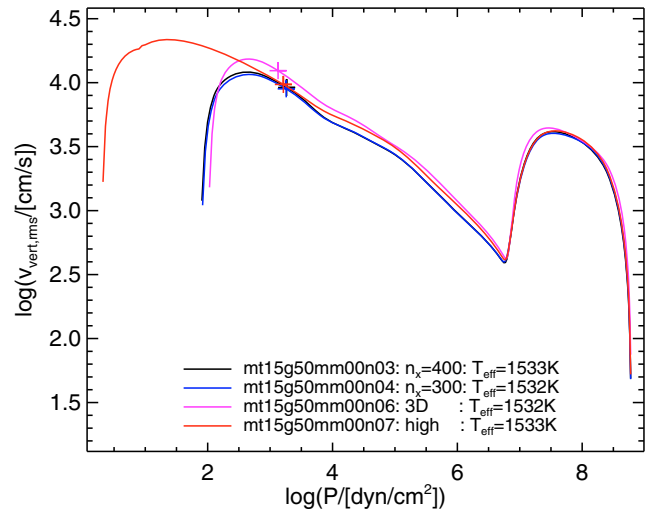
Fig. 12. The rms value of vertical velocity versus logarithm of pressure for models with $T_{\rm eff} \approx 1500$ K, $\log g = 5$, but differences in the geometry (horizontal grid points, vertical extent, dimension).

for the outermost layers, but remain negligible for determining the mixing mechanisms in these atmospheres.

Figure 12 shows the rms velocity for four 1500 K runs with different positions of the upper boundary. As expected, the more extended model has a larger peak velocity, while the agreement between the two curves is good in the lower atmospheric layers and excellent in the convection zone. We tried the same experiment at $T_{\rm eff} = 900$ K, 1200 K and, 2800 K with similar agreement between the pairs of curves.

Simulations that are not yet complete and that will be presented in future publications include a sequence with other gravity values that shows no qualitative change in the outcome, although convective velocities, wave amplitudes, and dust-formation rate equations noticeably depend on gravity: the dependence of the flow field and the cloud thickness on effective temperature will be different at other gravities.

A 3D model with $T_{\rm eff} = 1500$ K (after taking about half a year to cover 4 h of stellar time with six CPUs) has completed the transition from the initial 2D configuration to a fully 3D flow pattern. We see only small changes in the wave amplitudes and

convective velocities relative to a 2D run (Fig. 12). The 3D model data are in close agreement with the 2D models in the scatter plots in Fig. 10. Only its overshoot scale height (bottom right panel, $H_v = 0.2\,H_p$) is noticeably smaller than the average of the 2D models at $T_{eff} = 1500$ K ($H_v = 0.3\,H_p$).

The exploration of other parameters such as grain size and other types of dust awaits further simulations, using a more detailed cloud model (multi-size-bin scheme, in preparation).

4.2. Comparison with previous simulations

Ludwig et al. (2002, 2006) studied the structure of mid M-type, dust-free atmospheres including the mixing properties of macroscopic flows with 3D hydrodynamical simulations. Our $T_{eff} \approx 2800$ K model coincides in temperature with the coolest model of Ludwig et al., and this allows a comparison with the results. While the maximum rms vertical velocities in the convectively unstable layers turn out to be similar, the atmospheric-wave-dominated velocities are about 50% higher in Ludwig et al. Importantly, the scale height of the decline in the convective velocity field amplitude into the stably stratified layers is found to be similar ($H_v/H_p = 1.2$ this work, 1.1 in the work of Ludwig et al.). At first sight, this may appear surprising considering the systematic differences expected between simulations conducted in 2D and 3D as discussed by Ludwig & Nordlund (2000): in 2D the efficiency of wave generation is usually higher, and the transition between convectively stable and unstable regions is more gradual. However, the work of Ludwig & Nordlund refers to higher Mach-number flows, and pressure waves, not gravity waves, which are relevant here. In the higher Mach-number conditions studied by Ludwig & Nordlund, towards lower Mach-numbers the sharpness in the stable-unstable transition becomes more similar in the 2D and 3D simulations, so that the similarity in the M dwarf regime appears plausible. This is also borne out by a comparison with a 3D model compiled for 2800 K, which has a very similar velocity profile to its 2D counterpart.

Ludwig and collaborators had reasons to believe that the gravity waves present in their models were an artifact of the lower boundary condition. Moreover, they argued that the mixing efficiency is too small – because of both low (i.e., linear) amplitude and the insufficient shearing – to produce small-scale turbulence due to Kelvin-Helmholtz instabilities. Since in their models, convective overshoot was potentially able – when extrapolated to lower T_{eff} – to keep dust grains in the optically thin layers, they took assumed that waves are not important and convective overshooting is sufficient to explain the presence of dust clouds in brown dwarfs.

The present calculations cover the actual parameter regime of dust harbouring atmospheres. They show that – in contrast to expectations motivated by hotter models – convective overshoot alone is not capable of keeping dust grains in the atmosphere. Overshooting motions decline more rapidly towards lower effective temperatures (Fig. 10). Our thorough investigation of the influence of the boundary conditions on the excitation of the gravity waves indicate that they are indeed intrinsic to the flow evolution proper and not a numerical artifact. The gravity waves's ability to mix is indeed low but the waves remain in our hotter local models nevertheless the most efficient process, accompanied by dust convection in the case of heavy dust formation. All in all, we consider our present results consistent with the findings of Ludwig et al. (2002, 2006), but reassign the importance to the mixing by waves.

A complementary approach to ours is pursued by Helling et al. (2004): rather than on macroscopic scales (pressure scale heights, depth of the atmosphere, granular diameter), they concentrate on mesoscopic scales. Their 2D model is about as large (500×500 m^2) as one of our grid cells. They investigate the influence of driven turbulence, represented by a set of imposed pressure waves, on the formation of dust, particularly in regions where the temperature is slightly too high ($T = 2100$ K) to allow nucleation in an undisturbed atmosphere. We agree with their findings that fluctuations in the thermodynamic quantities can have an influence on the dust formation process. However, we identify gravity waves and not pressure waves as important contributors to the mixing in BD and M dwarfs, in addition to with convection within thick clouds and convective overshoot very close to the underlying gas convection zone. An important parameter in their simulations is the Mach number of the induced acoustic waves, for which they assume values of about 0.1 in 1D models and 1 in 2D models. However, peak convective Mach numbers (taking vertical and horizontal velocities into account) in our models are between 0.1 and 0.01, and rapidly decrease in the overshoot regions where high-temperature dust might form. The amplitude of turbulent structures on the grid cell scale and below – that we obviously cannot resolve in our models – would be even smaller. And only a tiny fraction of the energy can be expected to be transformed into pressure waves under these nearly incompressible low-Mach-number conditions. Therefore, based on our simulations we cannot justify the assumption of almost sonic pressure waves in the atmospheres of brown dwarfs as made in Helling et al. (2004).

4.3. Diffusion coefficient estimate

One can model the mixing of material by macroscopic flows – on average – as a diffusion process. However, in the hydrodynamical models there is a correlation between the sign of the vertical motions (upward of downward) and the grain growth. At the same velocity amplitude, the mixing efficiency of convective overturning flows is also much higher than that of (nearly reversible) wave motions, causing errors in the translation from the rms velocities to the actual mixing efficiency. The mixing efficiency can however be estimated from the rms vertical velocity of our model sequence as in Eq. (5). And the diffusion coefficient can be estimated from the local vertical velocity and the pressure scale height H_p as typical length scale via

$$D \propto V H_p. \tag{6}$$

However, the waves have a varying amplitude with height and therefore the typical length scale is not constant. On the other hand, their period is rather close to the Brunt-Väisälä period, which can be used as a characteristic timescale. Using the similar acoustic period, $t_{ac} = 2\,H_p/c_{sound}$, we obtain

$$D \propto V^2 t_{ac} \propto \mathrm{Ma}\,V H_p, \tag{7}$$

where the Mach number $\mathrm{Ma} = V/c_{sound}$. To take into account the increase in mixing with increase in non-linearity, one could multiply with the Mach number again to obtain

$$D \propto \mathrm{Ma}^2 V H_p. \tag{8}$$

Profiles for the diffusion coefficients according to the Eqs. (6)–(8) (replacing "$\propto$" by "=") are displayed in Fig. 13. Additional crosses mark estimates based on the horizontal and temporal averages of vertical flux and density profiles of dust plus monomers. Because the flux is divided by the vertical derivative of the concentration, which can be very small, these values are not well-behaved everywhere.
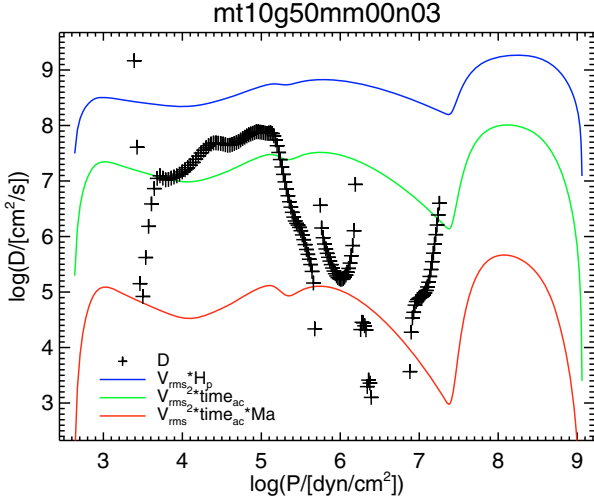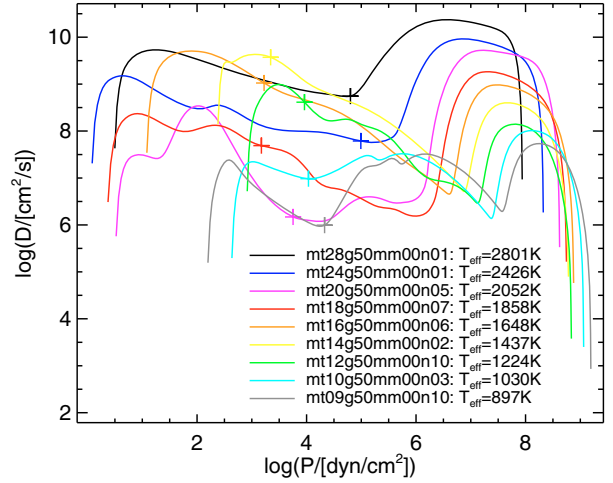
Fig. 13. Logarithm of diffusion coefficient versus logarithm of pressure for a model with T_{eff} = 1000 K according to Eqs. (6) to (8). The black crosses indicate estimates derived from the the averaged vertical fluxes and concentrations of dust and monomers.

Fig. 14. Logarithm of diffusion coefficient D (or K_{zz}) according to Eq. (7) versus logarithm of pressure for the same set of models as in Fig. 9.

Fig. 15. Logarithm of relative bolometric flux intensity contrast plotted versus effective temperature for all models in Table 1. *Top curve (circles)*: total contrast (spatial plus temporal contribution). *Bottom curve (plus signs)*: temporal variations only.

The diffusion coefficient in brown dwarfs is not a "constant of nature" but depends on the physical process driving the mixing, the height in the atmosphere, and the effective temperature. A lower gravity would lead (via increased convective velocities and larger time and spatial scales) to high diffusion coefficients.

Scaling relations such as Eqs. (7) and (8) can serve as a first step in describing the diffusion properties in ultracool atmospheres in greater detail. In addition, they can easily be translated into classical atmosphere codes. In an earlier study, we have implemented a non-equilibrium chemistry model in the PHOENIX BT-Settl code, using the diffusion coefficients derived from the overshoot contribution of the RHD simulations only. In atmosphere models of the T1 brown dwarf ε Indi Ba based on this approach, we obtain characteristic values of $10^7 \leq D \leq 10^8$ cm^2 s^{-1} for the transition region from CO- to CH$_4$-dominated carbon chemistry. We found the resulting non-equilibrium abundances of CO in the line-forming region, using an updated and more efficient reaction model than Saumon et al. (2006), to just slightly underestimate the observed CO line strengths in this benchmark transition dwarf (King et al. 2010). This indicates that somewhat more efficient mixing than provided by overshoot alone is required, thus supporting an additional contribution from gravity waves. The latest revision of the BT-Settl models being tested to include the effect of both dust mixing and CE departures, also find that Eq. (7) provides a close match to observational constraints.

In a more phenomenological approach Saumon et al. (2006) and Stephens et al. (2009) explored the effects of a constant eddy diffusion coefficient above the Schwarzschild boundary on observable departures from nitrogen and carbon equilibrium chemistry. They found best-fit values ranging from 10^2 to 10^6 cm^2 s^{-1}, although based on slower reaction rates (see above). Allowing for the differences in the reaction scheme, their results thus agree with the range of values that we find for the diffusion coefficient (crosses in Fig. 13) in the region spanning the top of the overshoot layers, the gravity-wave region, and the base of the cloud layers ($7.2 > \log P > 5.5$). Within the clouds, we find larger values.
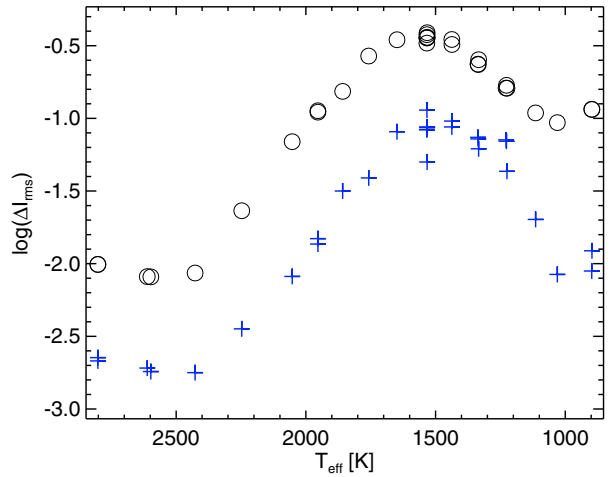
4.4. Brightness variations

Our simulations show temporal intensity variations for a wide range of timescales from half a minute to hours. We find low-amplitude (less than 1%, see Fig. 15) and short-period variability (1 min) due to the gravity waves producing temperature fluctuations and modulating the dust density and the vertical thickness of the clouds. Relatively short-lived (several minute) phenomena are the occasional dredge-up or outburst of material above the clouds, where dust falls back rapidly while monomers remain much longer. In the coolest models, the gravity waves are less visible in the intensity fluctuations, which are dominated instead by aperiodic variations on the scale of hours with an amplitude of a few per cent. But these results barely reach the scales of the observed variability of L-type brown dwarfs, which is often aperiodic (scales of hours to days) and of low amplitude (mmag) as reported by Gelino et al. (2002). Still, the spatial intensity contrast found in the models (Fig. 15) with significant dust layers is significantly higher than the contrast that would be induced by granulation alone (the small contrast for models above about 2500 K).

Our results are only those for a patch of the surface and the variability amplitudes obtained will average over the rest of the surface. To determine the brown dwarf surface distribution of clouds, one must go beyond the present simulations to 3D models that are as large as possible and include rotation effects.

We have neglected the effects of rotation despite the short rotational periods of brown dwarfs ($P \leq 4$ h). The convective turnover time in the box is several minutes, which is short in comparison. Neither the surface granules, nor our rms velocities, should therefore be severely affected. But granules could move with a global meridional flow. Other global flows caused by rapid rotation may exist that could move the dust around.

A cloud cover disruption has indeed been suggested as a possible additional cause – the cloud layers sinking relative to the line forming layers – of the L-T spectral transition (Ackerman & Marley 2001) that could lead to weather phenomena and spectroscopic variability.

5. Conclusions

We have performed radiation hydrodynamics simulations with CO5BOLD of a sequence of brown dwarf atmospheres extending previous studies to lower temperatures. The numerical model includes a simple treatment of the formation and destruction of dust, as well as its gravitational settling and advection, and also the interaction with the radiation field.

We provide a fit to the rms velocity in the atmosphere that can be used to estimate the mixing. The convective velocities fall significantly from the peak value inside the convection zone to the top of the unstable layers, and even further into the overshooting region. However, the scale height of exponentially decreasing overshoot velocities is so small that they do not induce significant mixing in the cloud layers. Above a local minimum in the vertical velocities, gravity waves dominate in the hotter models with an amplitude and mixing efficiency that increase rapidly with height, enough to balance the gravitational settling of dust. The wave amplitude decreases with decreasing effective temperature. In the cooler models, the dust layers are thick enough to cause convection within the clouds leading to efficient mixing within the cloud layers.

Models with high effective temperatures (2500 K $< T_{\mathrm{eff}} < 2800$ K) show a high-altitude haze of optically thin forsterite clouds. At lower effective temperatures ($T_{\mathrm{eff}} < 1400$ K), thick and dense forsterite clouds exist but mostly below the visible layers, which are essentially depleted of the material that went into the dust. For intermediate effective temperatures, dust is an important opacity source in the atmosphere. This agrees with observations by Golimowski et al. (2004), which place i) the onset of important refractory element depletion, where both TiO and VO bands weaken in spectra because of condensation of titanium and vanadium, and greenhouse effects at about 2500 K; ii) the maximum greenhouse effects at about 1800 K (M to L transition); and iii) the transition between dust-rich and dust-free brown dwarfs (L to T transition) at around 1450 K. We therefore feel confident that the mixing efficiency determined by our simulations is adequate. Although an investigation of the spectral properties of the models exceeds the scope of this paper, the formulae that we provide for the velocity field will allow the discrimination between diverse cloud model assumptions for brown dwarfs and planetary atmospheres.

References

Ackerman, A. S., & Marley, M. S. 2001, ApJ, 556, 872
Alexander, D. R., Allard, F., Tamanai, A., & Hauschildt, P. H. 1997, Ap&SS, 251, 171
Allard, F., Hauschildt, P. H., Alexander, D. R., Tamanai, A., & Schweitzer, A. 2001, ApJ, 556, 357
Asplund, M., Ludwig, H.-G., Nordlund, Å., & Stein, R. F. 2000, A&A, 359, 669
Baraffe, I., Chabrier, G., Allard, F., & Hauschildt, P. H. 1995, ApJ, 446, L35
Belkacem, K., Samadi, R., Goupil, M. J., et al. 2009, A&A, 494, 191
Böhm-Vitense, E. 1958, ZAp, 46, 108
Burrows, A., Sudarsky, D., & Hubeny, I. 2006, ApJ, 640, 1063
Cushing, M. C., Marley, M. S., Saumon, D., et al. 2008, ApJ, 678, 1372
Dintrans, B., Brandenburg, A., Nordlund, Å., & Stein, R. F. 2005, A&A, 438, 365
Ferguson, J. W., Alexander, D. R., Allard, F., et al. 2005, ApJ, 623, 585
Fortney, J. J., Cooper, C. S., Showman, A. P., Marley, M. S., & Freedman, R. S. 2006, ApJ, 652, 746
Freytag, B., & Höfner, S. 2008, A&A, 483, 571
Freytag, B., Ludwig, H.-G., & Steffen, M. 1996, A&A, 313, 497
Freytag, B., Steffen, M., & Dorch, B. 2002, Astron. Nachr., 323, 213
Gadun, A. S., Hanslmeier, A., Pikalov, K. N., et al. 2000, A&AS, 146, 267
García, R. A., Turck-Chièze, S., Jiménez-Reyes, S. J., et al. 2007, Science, 316, 1591
Geballe, T. R., Saumon, D., Golimowski, D. A., et al. 2009, ApJ, 695, 844
Gelino, C. R., Marley, M. S., Holtzman, J. A., Ackerman, A. S., & Lodders, K. 2002, ApJ, 577, 433
Golimowski, D. A., Leggett, S. K., Marley, M. S., et al. 2004, AJ, 127, 3516
Goode, P. R., Strous, L. H., Rimmele, T. R., & Stebbins, R. T. 1998, ApJ, 495, L27
Hauschildt, P. H., Baron, E., & Allard, F. 1997, ApJ, 483, 390
Helling, C., Oevermann, M., Lüttke, M. J. H., Klein, R., & Sedlmayr, E. 2001, A&A, 376, 194
Helling, C., Klein, R., Woitke, P., Nowak, U., & Sedlmayr, E. 2004, A&A, 423, 657
Helling, C., Ackerman, A., Allard, F., et al. 2008a, MNRAS, 1310
Helling, C., Ackerman, A., Allard, F., et al. 2008b, MNRAS, 391, 1854
Höfner, S., Gautschy-Loidl, R., Aringer, B., & Jørgensen, U. G. 2003, A&A, 399, 589
Hurlburt, N. E., Toomre, J., & Massaguer, J. M. 1986, ApJ, 311, 563
King, R. R., McCaughrean, M. J., Homeier, D., et al. 2010, A&A, 510, A99
Leggett, S. K., Allard, F., & Hauschildt, P. H. 1998, ApJ, 509, 836
Leggett, S. K., Allard, F., Geballe, T. R., Hauschildt, P. H., & Schweitzer, A. 2001, ApJ, 548, 908
Ludwig, H.-G., & Nordlund, Å. 2000, in Stellar Astrophysics, ed. K. S. Cheng, H. F. Chau, K. L. Chan, & K. C. Leung, 37
Ludwig, H.-G., Allard, F., & Hauschildt, P. H. 2002, A&A, 395, 99
Ludwig, H.-G., Allard, F., & Hauschildt, P. H. 2006, A&A, 459, 599
Marley, M. S., Fortney, J., Seager, S., & Barman, T. 2007, in Protostars and Planets V, ed. B. Reipurth, D. Jewitt, & K. Keil, 733
Nordlund, Å. 1982, A&A, 107, 1
Robinson, F. J., Demarque, P., Li, L. H., et al. 2003, MNRAS, 340, 923
Rossow, W. B. 1978, Icarus, 36, 1
Ruiz, M. T., Leggett, S. K., & Allard, F. 1997, ApJ, 491, L107
Saumon, D., Marley, M. S., Cushing, M. C., et al. 2006, ApJ, 647, 552
Skartlien, R., Stein, R. F., & Nordlund, Å. 2000, ApJ, 541, 468
Steffen, M., Ludwig, H.-G., & Krüß, A. 1989, A&A, 213, 371
Stein, R. F., & Nordlund, Å. 2000, Sol. Phys., 192, 91
Stein, R. F., & Nordlund, Å. 2001, ApJ, 546, 585
Stephens, D. C., Leggett, S. K., Cushing, M. C., et al. 2009, ApJ, 702, 154
Tsuji, T. 2002, ApJ, 575, 264
Tsuji, T., Ohnaka, K., & Aoki, W. 1996, A&A, 305, L1
Vögler, A. 2004, A&A, 421, 755
Wedemeyer, S., Freytag, B., Steffen, M., Ludwig, H.-G., & Holweger, H. 2004, A&A, 414, 1121
Witte, S., Helling, C., & Hauschildt, P. H. 2009, A&A, 506, 1367
Woitke, P., & Helling, C. 2003, A&A, 399, 297
Young, R. E. 1998, J. Geophys. Res., 103, 22775